JOURNAL OF COMPUTATIONAL PHYSICS **84**, 57–75 (1989)

Development of the Mask Method for Incompressible Unsteady Flows

M. BRISCOLINI AND P. SANTANGELO

IBM ECSEC, European Center for Scientific and Engineering Computing,
Via Giorgione 159, I-00147 Rome, Italy

Received November 30, 1987; revised July 22, 1988

A new method is developed to solve 2-dimensional time dependent incompressible viscous flows in an arbitrary geometry. The Navier–Stokes equations are solved in primitive variables using a pseudospectral formulation. The geometry is introduced by directly forcing the velocity field near the boundaries. The method extends a similar computational technique introduced by Basdevant and Sadourny [1]. Some examples are shown to evaluate its efficiency and accuracy.

1. INTRODUCTION

Spectral methods have been usefully introduced to simulate homogeneous and isotropic incompressible flows at high Reynolds numbers [2]. They are more accurate and more efficient than finite difference and finite element methods since they do not introduce truncation errors in spatial derivatives and give an exponential convergence for infinitely differentiable periodic functions. These methods can be easily applied to simple geometries when it is possible to use the FFT algorithm; their use in more complex geometries is generally forbidden by the lack of knowledge of the eigenfunctions of the Laplacian and of a corresponding fast algorithm to expand a given function in series. For example, Chebyshev polynomials [3] can be used to solve the flow in a channel [4].

This paper proposes a method in which an arbitrary computational domain **C** is embedded into a larger rectangular one (see Fig. 1) where the set of the eigenfunctions is chosen for simplicity to be the Fourier base. The method treats the no-slip condition of the Navier–Stokes equations as a forcing term acting, at each time step, on the physical boundary ∂C; the forcing depends on the velocity field. This method appears to be as precise as the spectral one everywhere except near the boundaries where the accuracy is reduced to the finite difference level. The original idea of this method has been introduced by Basdevant and Sadourny [1]; here we discuss a new version of the method.

Some simulations of external and internal flows in different geometries will demonstrate the efficiency and accuracy of the method; Section 2 describes the mathematical and numerical model; Section 3 shows the practical strategy of enfor-

0021-9991/89 $3.00

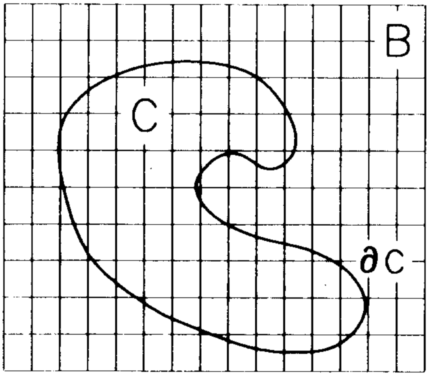

FIG. 1. The physical domain **C** is imbedded into the integration domain **B**.

cement of the boundary conditions; Section 4 contains the results of the simulation for the 2D driven-cavity and for the impulsively started flow around a cylinder at various Reynolds numbers.

2. MATHEMATICAL AND NUMERICAL MODEL

The Navier–Stokes equations in primitive variables, for an incompressible flow with constant density $\rho = 1$, are

$$\partial_t \mathbf{u} + (\mathbf{u} \cdot \nabla)\mathbf{u} + \nabla p = \nu \Delta \mathbf{u} + \mathbf{f}, \tag{1}$$

with the incompressibility equation

$$\nabla \cdot \mathbf{u} = 0, \tag{2}$$

where $\mathbf{u}(\mathbf{x}, t)$ and $p(\mathbf{x}, t)$ are the velocity field and the pressure respectively; ν is the viscosity and $\mathbf{f}(\mathbf{u}, \mathbf{x}, t)$ is the forcing term induced by the physical boundary $\partial\mathbf{C}$ and by any other external forcing.

The numerical integration proceeds according to the following three steps:

(a) free evolution of the velocity field inside the rectangular domain **B** neglecting forcing and pressure,

(b) introduction of the forcing term due to the boundary conditions on $\partial\mathbf{C}$,

(c) removal of the pressure by imposing the incompressibility of the field.

It is reasonable that this procedure gives a divergence-free field while satisfying exactly the boundary conditions as the time step and the mesh size approach zero.

The numerical spectral method used here is an explicit in time leap-frog scheme with exact resolution of the diffusive term. This is applied to Eq. (1) truncated to the maximum wavenumber K

$$\hat{\mathbf{u}}^{n+1} = e^{-\nu k^2 2\Delta t}\hat{\mathbf{u}}^{n-1} + 2\Delta t\, e^{-\nu k^2 \Delta t}(\hat{\mathbf{H}} + \hat{\mathbf{f}} - i\mathbf{k}\hat{\pi})^n, \tag{3}$$

where the hat labels the Fourier components and the superscripts refer to time $t_n = n\,\Delta t$. **H** is the non-linear pseudospectral term [2]; in two dimensions, **H** is calculated efficiently with the fourth formulation proposed by Basdevant [5] which requires four FFTs instead of the five FFTs of the standard expression; π is the total pressure. Equation (3) is integrated with a fractional-step time-advancing scheme [6, 7]. Step (a) gives the solution of the momentum equation:

$$\hat{\mathbf{u}}_a = e^{-\nu k^2 2\Delta t}\hat{\mathbf{u}}^{n-1} + 2\Delta t\, e^{-\nu k^2 \Delta t}\hat{\mathbf{H}}^n. \tag{4}$$

In step (b) the field $\hat{\mathbf{u}}_a$ is forced to obey the boundary conditions using the linear operator $\hat{P}$:

$$\hat{\mathbf{u}}_b = \hat{P}\hat{\mathbf{u}}_a. \tag{5}$$

Valid expressions for $\hat{P}$ will be specified in detail in Section 3. To work correctly the operator $\hat{P}$ must be a projector, at least in its continuous representation (i.e., when the mesh size approaches zero). In this respect (5) is equivalent to the formulation introduced by Basdevant and Sadourny [1]. In step (c) the incompressibility of the field is imposed removing the gradient of a scalar field ϕ from $\mathbf{u}_b$ as:

$$\hat{\mathbf{u}}^{n+1} = \hat{\mathbf{u}}_b - i\,2\Delta t\,\mathbf{k}\hat{\phi}, \tag{6}$$

where $\hat{\phi}$ is expressed by

$$\hat{\phi} = -\frac{i}{2\Delta t}\frac{\mathbf{k}\cdot\hat{\mathbf{u}}_b}{k^2}. \tag{7}$$

The three-step procedure indicated so far allows also for the explicit determination of the forcing and the pressure terms, respectively. This is given by substituting (4) in (5) and successively (5) in (6) using $P = 1 - M$. Expanding the exponential terms to first order and comparing with (3) one finally obtains the forcing term

$$\hat{\mathbf{f}}^n \simeq -\frac{\hat{M}\hat{\mathbf{u}}_a}{2\Delta t}(1 + \nu k^2\,\Delta t), \tag{8}$$

and the pressure

$$\hat{\pi}^n \simeq \hat{\phi}(1 + \nu k^2\,\Delta t). \tag{9}$$

The order of approximation in (8) and (9) is $o(\nu k^2\,\Delta t)$; this corresponds to a numerical boundary layer of thickness $\delta \sim (\nu\,\Delta t)^{1/2}$ (see Orszag *et al.* [8] for an extensive discussion). This layer is very dangerous for implicit in time finite difference schemes which use a large Δt [9], while it does not affect significantly our scheme which is explicit in time and thus requires a small time step [10].

3. TREATMENT OF THE BOUNDARY CONDITIONS

The practical method of forcing the boundary conditions in Eq. (5) is a key point of this work. This problem is an important one because the very use of an eigenfunction expansion imposes some constraints on the type of forcing which is necessary to model the boundary conditions. In fact, given a sufficiently regular velocity field, if one tries to set at will the value of the velocity on some collocation points (say on the boundary), then the corresponding Fourier analysis shows strong oscillations near those points. These oscillations are known as the Gibbs' phenomenon and have the unfortunate property that they do not vanish even when the mesh size goes to zero [11].

An efficient method to remove the unwanted and dangerous Gibbs' oscillations uses a procedure that spreads the boundary line into the narrow strip whose thickness is a few grid points. The broadened boundary line avoids the sharp setting of the values on the boundary, which is responsible for the oscillations. Indeed, one can thus exploit the new degree of freedom, locally perpendicular to the boundary, to decrease the forcing of the velocity field as one gets farther from the boundary line. The oscillations decrease in amplitude when the thickness of a strip increases. There are now two conflicting requirements because one needs both a thick strip to avoid large Gibbs' oscillations and simultaneously a thin one to maintain the boundary strip as localized as possible. It is shown in the following that these

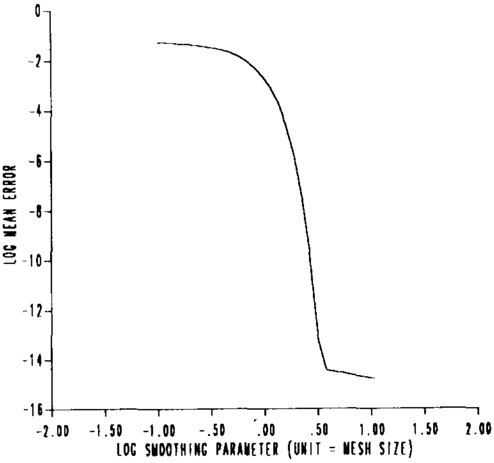

FIG. 2. Maximum value of Gibbs' oscillations for the error integral $\operatorname{erf}(x/\sigma)$ versus σ; note the sharp decrease of the Gibbs' phenomenon when σ is of the order of a few meshes.

requirements can both be met with a strip whose thickness is only 2–3 grid points. The use of a narrow strip in place of a thin boundary line has the further advantage of avoiding the necessity of having the boundary pass exactly through the collocation points.

To increase confidence in the proposed method two simple cases are shown where a function with a discontinuity is analyzed in Fourier series; in these cases the strength of the Gibbs' phenomenon is substantially reduced at the minor cost of a negligible smoothing of the original function.

In the first case one uses the step function whose Fourier analysis shows the Gibbs' phenomenon by definition; this simple discontinuous function is the limiting case of the error integral when the rms $\sigma \rightarrow 0$. Figure 2 reports the maximum value of the Gibbs' phenomenon versus the σ of the error integral; one sees that for very low values of σ one retrieves the Gibbs' phenomenon while a small $\sigma \sim 2\Delta x$ is sufficient to damp the amplitude of the oscillations by more than two orders of magnitude.

The second case is a more theoretical way of looking at the same procedure; this is given by the well known method of Lanczos' sigma factors which is often used to improve the convergence of slowly converging Fourier series [11]. The method consists in multiplying a given slowly converging series by Lanczos' series and can be shown to correspond to a fine scale smoothing of the non-transformed function [11]. For the simple step function, whose Fourier series slowly converges at order $o(N^{-1})$, Lanczos' sigma factors improve the convergence up to $o(N^{-2})$ [12]. Furthermore, the simple example of the step function can be used to show that Lanczos' method gives a finite difference accuracy for the evaluation of the derivatives [12] near the point of maximum steepness while it maintains the spectral accuracy elsewhere. In both cases one sees immediately the similarity with our method which is essentially a smooth way of enforcing the boundary conditions.

Two different practical strategies of implementation of the operator P for a no-slip boundary are shown in the following.

First Forcing Method

Let us define a function $M_{\mathrm{nr}}(x, y)$ (nr = *narrow mask*) which is zero inside the given flow domain **C** and is one elsewhere with a smooth connection of the two values; Fig. 3 is an example of such a function for an impenetrable disk inside a rec-

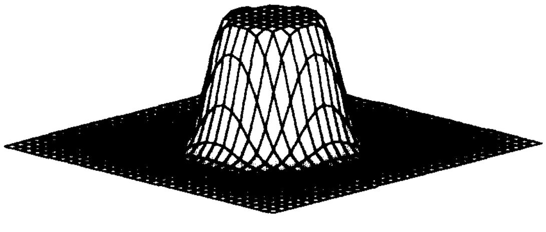

FIG. 3. The *narrow mask* M_{nr} for an impenetrable disk.

tangular domain. In this case the projection operator P is the simple multiplicative function

$$P = 1 - M_{\mathrm{nr}}; \tag{10}$$

the operation shown in (5) is a convolution in Fourier space and is performed conveniently with a multiplication in the non-transformed space at the minor cost of some additional FFTs.

A similarly working definition of M_{nr} is zero inside the given flow domain **C** and is peaked to one only near the boundary with a smooth connection between the two values. At variance with the previous definition of M_{nr} (which is one outside **C**) the flow could now show the development of a spurious fluid movement outside the computational domain.

Some tests have shown that a gaussian shaped function with rms σ_{nr} is an economic and reasonable choice for the shape of M_{nr} near the boundaries. It is interesting to analyze the effects of this type of forcing; to this end, and for the sake of simplicity, we write explicitly the unidimensional version of (5) in the non-transformed space; the formula is: $u_b(x) = (1 - M_{\mathrm{nr}}(x))\, u_a(x)$. One recognizes immediately that, for any $M_{\mathrm{nr}}(x)$, which is flat near the boundary, not only the velocity u_b but also its spatial derivative tend to zero near the boundary itself. The same applies in two dimensions and this is rather unfortunate because the value of the velocity derivatives at a no-slip wall are generally different from zero.

Second Forcing Method

A second form of the operator P forces only the velocity while leaving almost untouched the velocity derivatives; this is important near the no-slip wall if one wants to solve in some detail the boundary layer. In this case P is given by the two formulae

$$\tilde{\mathbf{u}} = M_{\mathrm{nr}} \mathbf{u}_a, \tag{11}$$

and

$$\mathbf{u}_b = \mathbf{u}_a - M_{\mathrm{br}} \otimes \tilde{\mathbf{u}}, \tag{12}$$

where the symbol $\otimes$ indicates the spatial convolution with a second gaussian mask M_{br} (br = *broad mask*) given by

$$M_{\mathrm{br}}(x, y) = \frac{1}{2\pi\sigma_{\mathrm{br}}^2}\, e^{-(x^2 + y^2)/2\sigma_{\mathrm{br}}^2}, \tag{13}$$

where σ_{br} is somewhat (generally two times) larger than σ_{nr}. The convolution is directly computed with a product in Fourier space. The analysis of the effect of this second type of forcing is now performed again in the unidimensional case for simplicity; it gives: $du_b/dx = du_a/dx + \sigma(\Delta x)$. Hence the velocity derivatives of u_b on the boundary are no longer zero. Experimentation with different values of the parameters σ_{nr} and σ_{br} has shown that the smallest values which give almost no oscillations are $\sigma_{nr} = 0.5$ and $\sigma_{br} = 1$ when measured in units of grid points.

The key parameter of the second forcing method is σ_{br} which rules the strength of Gibbs' phenomenon (as in Lanczos' method) while σ_{nr} (the width of the boundary strip) is only used to allow for the case of a boundary line which does not pass exactly through the grid points.

A comparison between the two types of forcings is clearly shown in Figs. 4 and

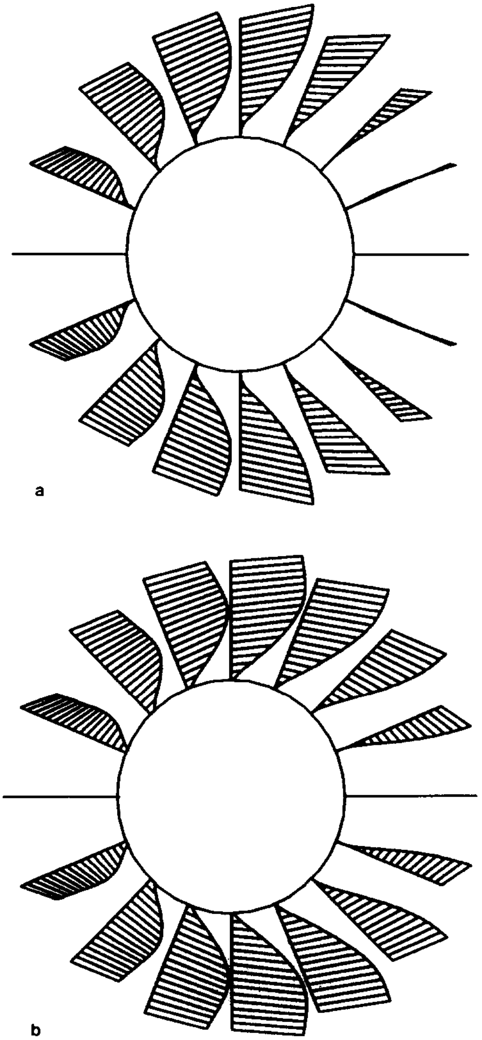

FIG. 4. Velocity profile around a circular cylinder in a uniform flow at Re = 20 with the first forcing (a) and for the second forcing (b).

favors the second method since it does not force to zero the velocity derivatives on the wall. Only the second forcing method will be used throughout the rest of the paper.

This practical strategy of enforcement of the boundary conditions is easily extendible to the case of a non-zero velocity on the boundary; to this end formula (11) is replaced by

$$\tilde{\mathbf{u}} = M_{\mathrm{nr}}(\mathbf{u}_a - \mathbf{V}), \tag{14}$$

where the field $\mathbf{V}$ is the assigned boundary velocity. A proper operation of the algorithm requires that the value of $\mathbf{V}$ on the boundary is nearly constant over length scales larger than σ_{nr}.

It seems that an important disadvantage of the mask method is the necessity to pay off a large number of grid points over the whole computational domain in order to resolve sufficiently well the boundary zone; this is true for stationary flows where the fluid patterns are simple. The situation is completely different for non-stationary flows whose motion is almost unpredictable and thus require a fine meshing everywhere. In this case the uniformity of the meshing of our mask method is no more a serious problem but rather combines well with the highly regular memory structure of the present supercomputers so that a clear trade-off can be easily recognized in favor of the mask method which furthermore offers the possibility to change arbitrarily the boundary conditions. In particular, the complete mask method (comprising field evolution and enforcement of the boundary conditions) is fully vectorizable and parallelizable and can be exploited both in two and three dimensions on present virtual memory machines. All the computations shown in this paper have been performed on an IBM 3090 vector multiprocessor with a fully parallel in core code.

4. Results and Discussion

The present section contains the results of some simulations of 2-dimensional flows using the second forcing method. Two cases have been selected: the flow in a square cavity driven by a moving wall and the flow past a circular cylinder embedded in a uniform flow. The former is an example of a recirculating internal flow with strong discontinuities while the latter is an example of an external separated flow over a bluff body.

2D Driven-Cavity Flow

The driven-cavity test is often used to check numerical methods for incompressible fluid flows [13, 14, 9]. In this example the recirculation region is induced by the moving wall and diffuses inside the cavity. The test has been selected because the flow pattern depends sensitively on the Reynolds number, as has been clearly shown by Ghia *et al.* [14] who use a multigrid method to solve the flow.

The geometry of the mask for the cavity flow is as follows: with reference to Fig. 1 the cavity with side L is the physical domain which is centered in a larger computational square with side $L_x = 1.28L$. The mask field M_{nr} is peaked on the four sides of the cavity and is zero elsewhere; the field $\mathbf{V}$ is non-zero only on the upper side and its value is U. The Reynolds number of this flow is $\mathrm{Re} = UL/\nu$. Two flows with $\mathrm{Re} = 100$ and $\mathrm{Re} = 400$ are computed with a 128×128 grid; this corresponds to 100×100 grid points for the cavity. (Since the *broad mask* has a

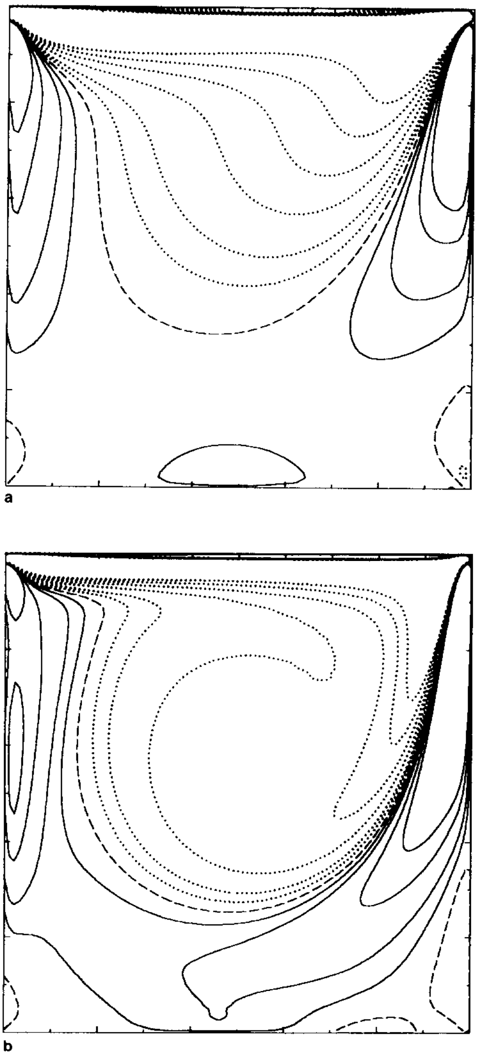

FIG. 5. Vorticity field in a driven-cavity; the computational grid is 100×100 and the Reynolds number is 100 in (a) and 400 in (b). The vorticity levels are: $+0.5$, $+1$, $+2$, $+3$ (continuous lines), -0.5, -1, -2, -3, -4, -5 (dotted lines), and 0 (dashed line) [14].

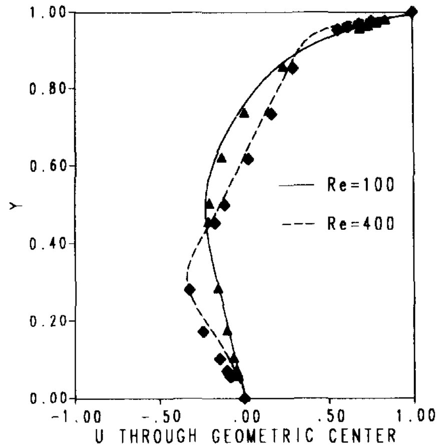

FIG. 6. Horizontal velocity profile along the median vertical line at Re = 100 and Re = 400. Comparison between present results (lines) and Ghia *et al.*'s [14] results (symbols).

gaussian shape, the largest cavity that could be computed has side $L \sim L_x - 6\sigma_{\mathrm{br}}$). The time step is selected according to the two linear stability criteria $\Delta t\, \nu/\Delta x^2 < 0.25$ and $\Delta t/\Delta x\, U < 1$: $\Delta t = 10^{-3}$ meets them both.

The flow in the cavity is shown in Fig. 5a at $T = 20$ for Re = 100 and in Fig. 5b at $T = 50$ for Re = 400 when both flows appear to be completely developed; the flow patterns compare remarkably well with the results of Ghia *et al.* [14] who use a 129 × 129 grid for their multigrid computations; minor differences of the vorticity patterns appear only near the lower corners.

The vertical and horizontal velocity profile through the cavity center are shown in Figs. 6 and 7, respectively, where they are checked against published results

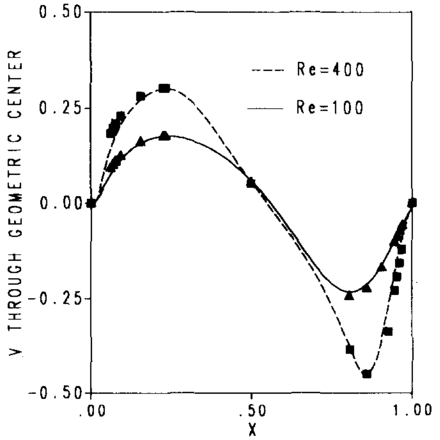

FIG. 7. The same as in Fig. 6 but for the vertical velocity profile along the median horizontal line.

[14]; the comparison is qualitatively good near the moving wall. A small difficulty is shown by the case with $\mathrm{Re} = 400$ near the center of the lower wall where the value of the vorticity is smaller than the expected one [14]; this is probably due to insufficient resolution.

Impulsively Started Flows around Cylinders

Laminar flows. The flow past a circular cylinder has been chosen to verify the ability of the mask method to solve viscous flows in contact with a curved wall. This flow presents a recirculation region behind the body (the wake) that increases with the Reynolds number (stable laminar regime) up to the critical value $\mathrm{Re}_c \sim 70$ [15]; when $\mathrm{Re} \sim \mathrm{Re}_c$ the flow starts to show an oscillating wake while a Karman vortex street with a strong separation appears for $\mathrm{Re} \gg \mathrm{Re}_c$ (turbulent regime).

The flow is integrated in the whole domain without any symmetry enforcement and with periodic boundary conditions in the vertical direction; this is obtained using a mask M_{nr} which is peaked on the wall of the cylinder. The Reynolds number is $\mathrm{Re} = 2UR/\nu$, where R is the radius of the circular cylinder and U is the uniform incoming velocity. The sides of the rectangular domain are $L_x = 16R$ and $L_y = 8R$, the grid is 256×128, and the time step is $\Delta t = 2.5 \times 10^{-3}$. Case B at $\mathrm{Re} = 40$ (see the Table I) is different: $L_x = L_y = 16R$ and the grid is 256×256. The center of the cylinder is 12 radii far from the right outflow side; this is sufficient to ensure a negligible perturbation of the boundary on the wake for Reynolds numbers up to 70 when the length of the wake is of order $8R$ [16]. The left and right vertical sides are treated as boundary segments with the assigned velocity $\mathbf{V} = (U, 0)$ and the corresponding masks M_{nr} and $\mathbf{V}$ are set accordingly: this procedure is able to destroy the vorticity patterns exiting from the computational domain and ensure a uniform inflow (see Figs. 8 and 10). No conditions are imposed on the lower and upper sides of the domain and the computation is fully periodic along the vertical direction.

The flow has been computed for different Reynolds numbers in the range 20–1000; Figs. 8 show the vorticity fields for these computations at time $T = 16$. The

TABLE I

Re	C_D	$p(\pi)$	$-p(0)$	Φ	$L_w/2R$
20.	2.79	1.27	1.27	40.	0.90
40.	1.93	1.13	0.91	51.	2.19
40 B	1.74	1.08	0.80	51.	2.19
60.	1.61	1.09	0.80	57.	2.96
80.	1.44	1.08	0.73	59.	3.41*
100.	1.33	1.07	0.68	65.	3.90*
200.	1.10	1.07	0.55	80.	—
500.	0.90	1.07	0.25	88.	—
1000.	0.82	1.06	0.06	86.	—

Note. Starred values are measured at $T = 80$.

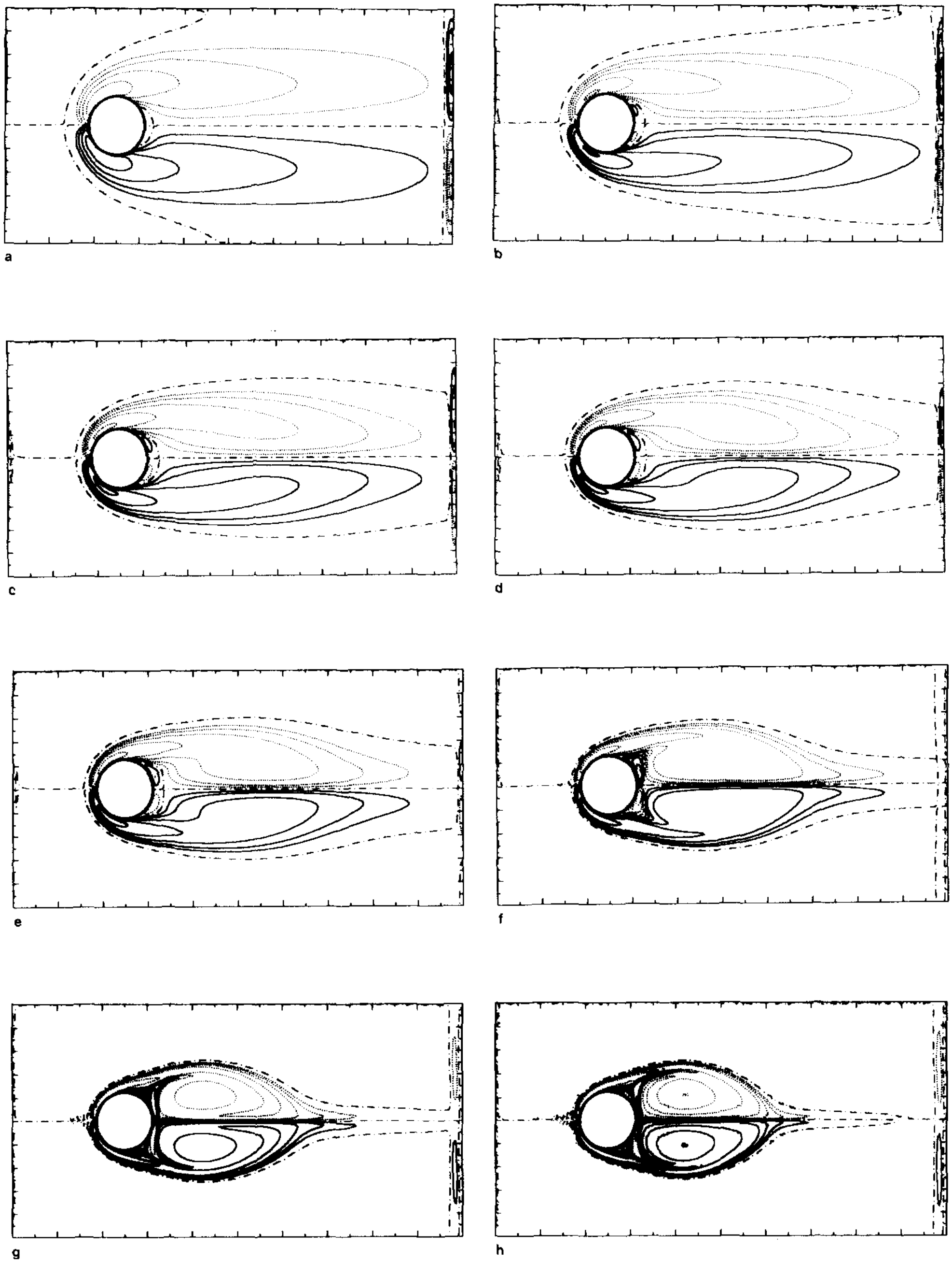

FIG. 8. Vorticity field for an impulsively started flow around a circular cylinder using a 256×128 grid. The vorticity values are $+5$, $+2$, $+1$, $+0.5$, $+0.25$ (continuous lines), -5, -2, -1, -0.5, -0.25 (dotted lines), and 0 (dot-dashed line). Time is $T = 16$ and the Reynolds number is (a) $Re = 20$; (b) $Re = 40$; (c) $Re = 60$; (d) $Re = 80$, (e) $Re = 100$; (f) $Re = 200$; (g) $Re = 500$; (h) $Re = 1000$.

pictures show clearly that the mask of the cylinder does not perturb appreciably the flow near the obstacle. The vorticity does not attain its maximum value on the wall of the cylinder but only at the *effective radius* that is found experimentally as $R_{\text{eff}} \equiv R + 3\sigma_{\text{nr}}$. Note, however, that this is only 1.5 grid points outside the cylinder for our choice of $\sigma_{\text{nr}} = \Delta x/2$. Figs. 9a and b show the vorticity and pressure field at R_{eff}: it is apparent that the maximum value of vorticity decreases excessively at high Reynolds number as an effect of the low space resolution near the cylinder.

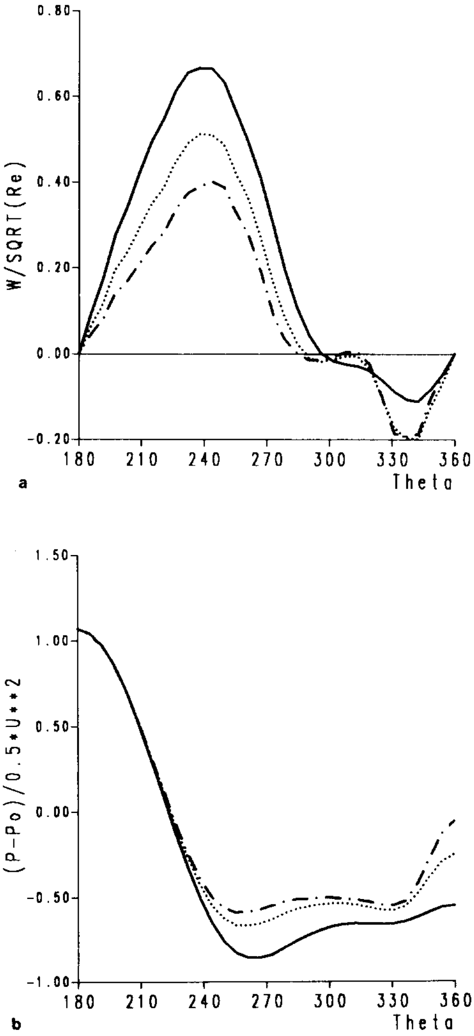

FIG. 9. Vorticity field at *effective radius* R_{eff} as a function of the angle from leading edge of the flow; the time is $T = 16$ and the Reynolds number is 200 (continuous line), 500 (dotted line), and 1000 (dot-dashed line). The same in (b) but for the pressure.

Table I reports some relevant quantities of the flows. These are: (a) the drag coefficient

$$C_D = -\frac{1}{2}\int_0^{2\pi} p\cos\theta\, d\theta - \frac{2}{\mathrm{Re}}\int_0^{2\pi} \partial_n\omega \sin\theta\, d\theta, \tag{15}$$

where ω is the vorticity and the integration is performed on the surface of the cylinder (∂_n is the normal derivative on the wall); (b) the stagnation pressure

$$p(\pi) = 1 - \frac{2}{\mathrm{Re}}\int_0^{x_s} \partial_y\omega\, dx \tag{16}$$

where the integral is performed on the axis line from the inflow edge $x = 0$ to the stagnation point x_s; (c) the pressure behind the body $p(0)$; (d) the separation angle Φ; and (e) the wake length $L_w/2R$ in units of the diameter of the cylinder.

The values in the table are calculated at $T = 16$; this is appropriate for flows with $\mathrm{Re} \leqslant 60$ that reach a steady configuration by that time with a wake that fits well within the integration domain. In the case of flows with larger Reynolds numbers the wake should extend beyond the outflow boundary and time $T = 16$ is a compromise between the opposing needs of an evolving flow and for a negligible influence of the outflow boundary on the wake. The values of the table have been checked against many numerical computations for the flow past a cylinder in an infinite domain [17–20]; the main result of the comparison is that the stagnation pressure and the separation angle agree with the published data at the 5% level while the pressure behind the body is significantly different, probably as a consequence of the finite extent of our computational domain. The length of the wake is accurate as long as the wake remains sufficiently far from the right side of the integration region ($\mathrm{Re} = 40$). The value of the drag of simulation B at $\mathrm{Re} = 40$ is in good agreement with Rosenfeld and Wolfshtein [20] who solve the flow for a periodic vertical array of circular cylinders; in the other cases the vertical periodicity of our computational domain causes the drag coefficient to be about 30% different with respect to results obtained by other authors in an infinite domain [17–19].

Turbulent flows. At large Reynolds numbers $\mathrm{Re} \gg \mathrm{Re}_c \sim 70$ the wake is destabilized by any small asymmetric perturbation induced by the outflow boundary. When $\mathrm{Re} \geqslant 500$ this effect appears already for $T \geqslant 20$ while for $\mathrm{Re} = 200$ a weak instability appears only for much longer times ($T > 80$). Figures 10 show the development of the Karman vortex street for $\mathrm{Re} = 1000$; Figs. 10a and b give the early symmetric development of the wake that is perturbed around time $T = 50$ (Figs. 10c and d) when the wake touches the outflow side and eventually generates a Karman vortex street (Figs. 10e and f). The last two figures are four time units spaced and show two nearly symmetric flow configurations of the oscillating wake. These permit to estimate by eye the frequency of the oscillation $n \simeq \frac{1}{8}$ and consequently the Strouhal's number $S = n\, 2R/U \sim 0.25$. The same result is given by a

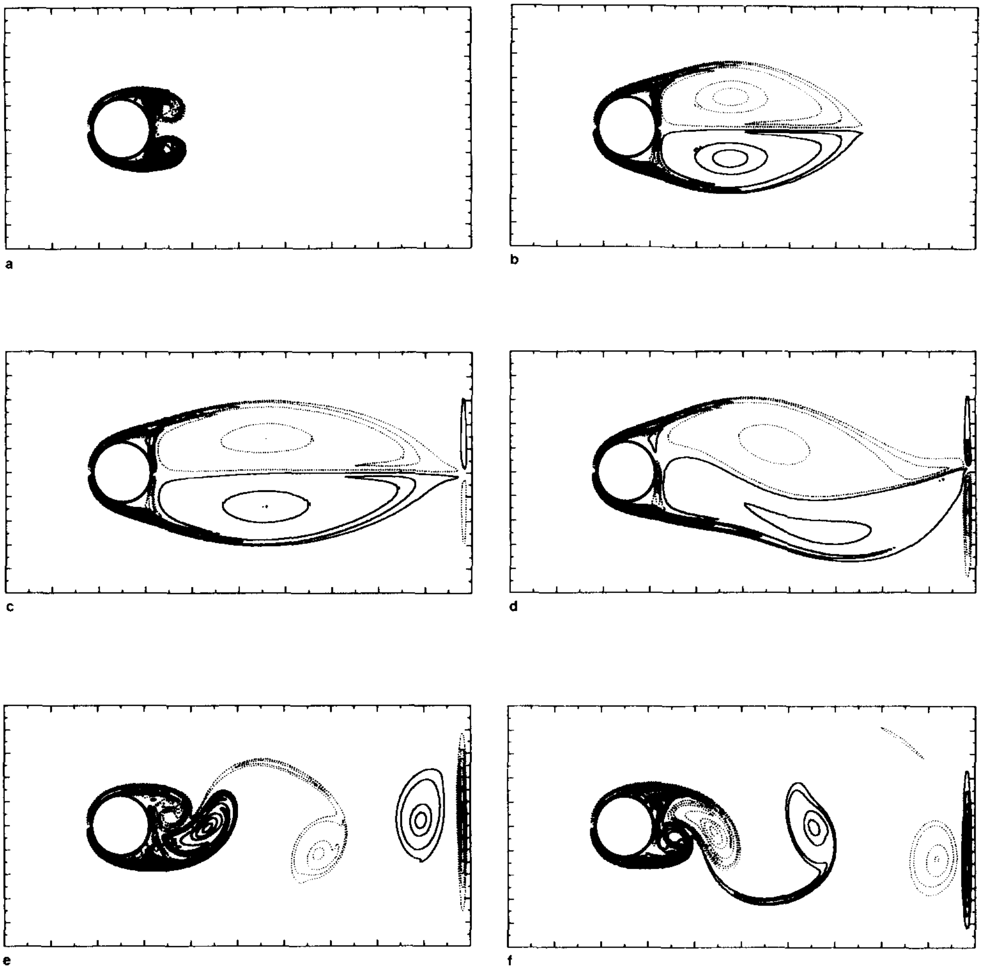

FIG. 10. Evolution of the vorticity field for an impulsively started flow around circular cylinder at Re = 1000 using a 256 × 128 grid. 11 vorticity lines are equally spaced in the range $-10 \div 10$; continuous (dotted) lines indicate positive (negative) vorticity; time is (a) $T=4$; (b) $T=28$; (c) $T=48$; (d) $T=56$; (e) $T=76$; (f) $T=80$.

more precise measurement which is based on the harmonical analysis of a long time record of the velocity field in two points inside the wake. Published estimates of the Strouhal's number give $S \simeq 0.21$ [21, 22] and are significantly smaller probably as a consequence of the vertical periodicity of the boundary conditions. The flow structure near the trailing edge of the cylinder is sufficiently accurate to show such important features as the secondary eddies (see Figs. 11); but finer details such as the α or the β-phenomena reported by Bouard and Coutanceau [16] for Re $\geqslant 800$ do not appear as a consequence of insufficient numerical resolution near the wall.

Figures 10d, e, and f show clearly that the right absorbing boundary of the domain is able to damp the outflow without contaminating the inflow. This is not trivial since the flow domain is doubly periodic.

The slight roughness of the contour lines for the flow past the cylinder shown in Figs. 11 is not the consequence of the Gibbs' phenomenon but rather the result of the use of a too small viscosity. This is shown by the fact that the small ripples are

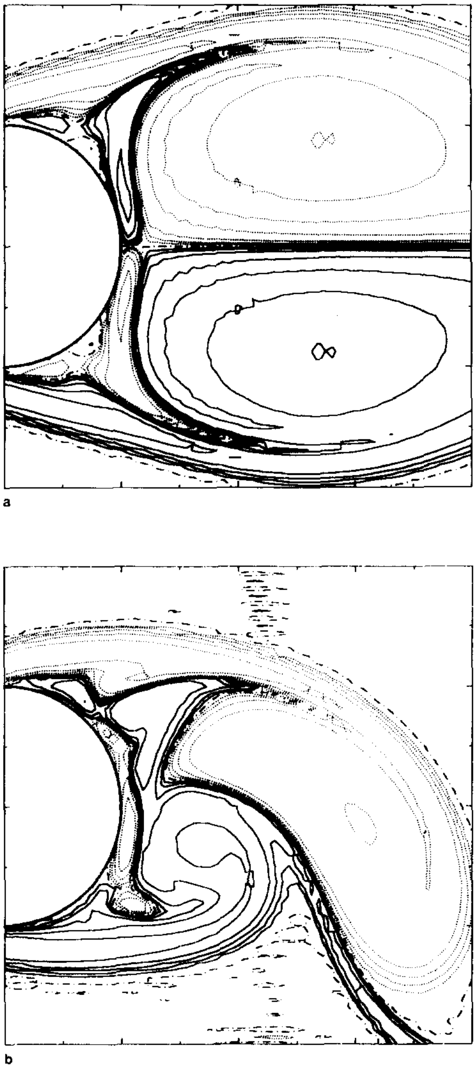

FIG. 11. An enlargement of the flow at Re = 1000 is shown near the trailing edge of the cylinder at time $T = 16$ (a) and $T = 80$ (b). The vorticity values are $+5$, $+2$, $+1$, $+0.5$, $+0.25$ (continuous lines), -5, -2, -1, -0.5, -0.25 (dotted lines), and 0 (dot-dashed line).

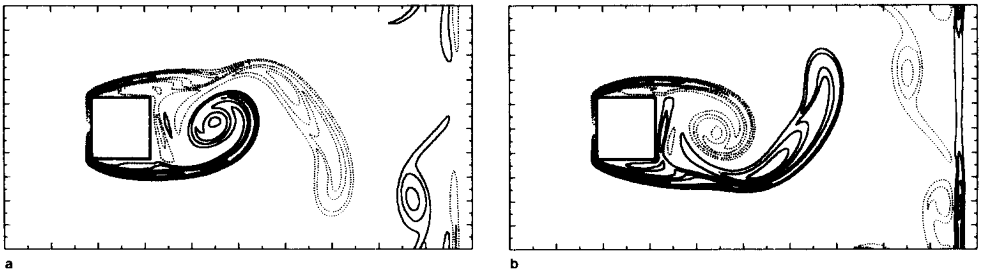

FIG. 12. The same as in Figs. 10 but for an impulsively started flow around a square at Re = 1000; time is $T = 156$ (a) and $T = 160$ (b).

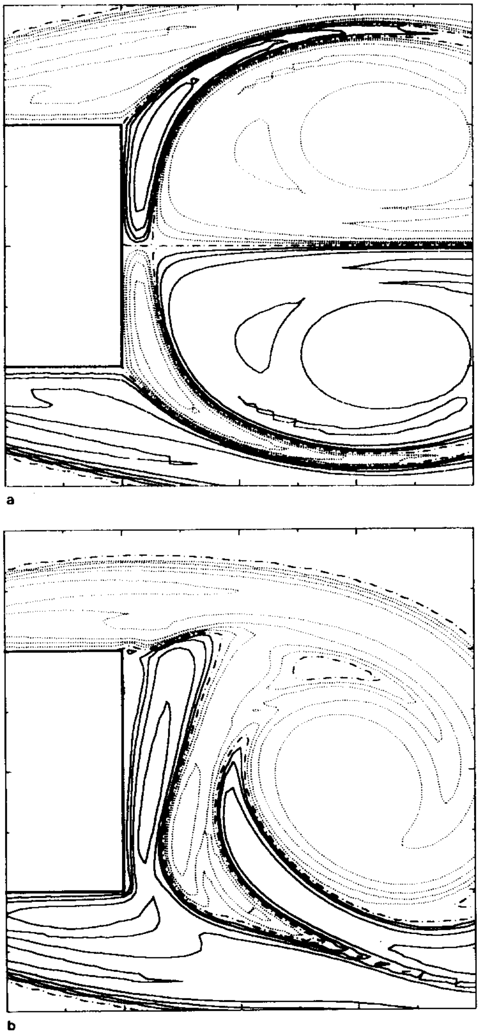

FIG. 13. The same as in Fig. 11 but for an impulsively started flow around the square cylinder at Re = 1000; time is $T = 16$ (a) and $T = 160$ (b).

recognizable only in experiments with very high Reynolds number (Re = 1000 in Figs. 11) and not in all other cases corresponding to lower Reynolds numbers.

As a final test for the mask method, the flow past a square cylinder [23] is investigated. This is shown in Figs. 12 for Re = 1000. The Strouhal's number based on the harmonical analysis of velocity time records is $S \simeq 0.21$, in agreement with the numerical results by Davis and Moore [23]. Figures 13 are enlargements of the flow near the rear side of the square. Note the remarkable ability of the mask method to deal with the sharp corners of the square.

5. Conclusions

The present paper develops a new computational method for 2-dimensional incompressible viscous flows in an arbitrary domain. The complexity of the geometry is handled by embedding the flow domain into a basic rectangular one and directly forcing the boundary conditions while the computations are performed straightforwardly in the rectangular domain using a spectral method. The technique is well suited for detached flows and shows a clear trade-off between simplicity and approximation. In fact, the method has the high accuracy of spectral ones almost everywhere while it is only a little less precise near the boundary where one expects a reduction of the accuracy to the finite difference level. The procedure is completely vectorizable and parallelizable and can very well exploit the presently available supercomputers. The use of the velocity–pressure formulations makes it easier to handle the boundary conditions and could be extended even to the 3-dimensional case. A similar computational technique has been used first by Basdevant and Sadourny [1] with the vorticity formulation of the Navier–Stokes equations. Here their method is extended to more difficult problems like the 2-dimensional driven cavity and a new technique is added to avoid the Gibbs' oscillations connected with the sharp boundary gradients.

Acknowledgments

The authors thank C. Basdevant, R. Sadourny, R. Benzi, and G. F. Carnevale for discussions and comments.

References

1. C. Basdevant and R. Sadourny, "Numerical simulation of incompressible flow: the Mask method," Laboratoire de Météorologie Dynamique Ecole Normale Supérieure, Paris, 1984 (unpublished).
2. S. A. Orszag, *Stud. Appl. Math.* **50**, 293 (1971).
3. S. A. Orszag, *J. Comput. Phys.* **37**, 70 (1980).
4. S. A. Orszag and L. C. Kells, *J. Fluid Mech.* **96**, 159 (1980).
5. C. Basdevant, *J. Comput. Phys.* **50**, 209 (1983).

6. A. J. Chorin, *Math. Comput.* **23**, 341 (1969).
7. R. Temam, *Navier-Stokes Equations. Theory and Numerical Analysis*, 2nd ed. (North-Holland, Amsterdam, 1979).
8. S. A. Orszag, M. Israeli, and M. O. Deville, *J. Sci. Comput.* **1**, 75 (1986).
9. J. Kim and P. Moin, *J. Comput. Phys.* **59**, 308 (1985).
10. R. Peyret and T. D. Taylor, *Computational Methods for Fluid Flow*, Springer Series in Computational Physics (Springer-Verlag, Berlin, 1983).
11. C. Lanczos, *Applied Analysis* (Prentice–Hall, Englewood Cliffs, NJ, 1956).
12. F. Scheid, *Numerical Analysis* (McGraw–Hill, New York, 1968).
13. K. Goda, *J. Comput. Phys.* **30**, 77 (1979).
14. U. Ghia, K. N. Ghia, and C. T. Shin, *J. Comput. Phys.* **48**, 387 (1982).
15. J. K. Batchelor, *An Introduction to Fluid Dynamics* (Cambridge Univ. Press, London, 1967).
16. R. Bouard and M. Coutanceau, *J. Fluid Mech.* **101**, 583 (1980).
17. C. R. Dennis, *J. Fluid Mech.* **42**, 471 (1970).
18. S. Tuann and M. D. Olson, *Comput. Fluids* **6**, 219 (1978).
19. V. A. Patel, *Comput. Fluids* **4**, 13 (1976).
20. M. Rosenfeld and M. Wolfshtein, *Comput. Fluids* **12**, 293 (1984).
21. S. K. Jordan and J. E. Fromm, *Phys. Fluids* **15**, 371 (1972).
22. Y. Lecointe and J. Piquet, *Comput. Fluids* **12**, 255 (1984).
23. R. W. Davis and E. F. Moore, *J. Fluid Mech.* **116**, 475 (1982).